


Na-functionalized IrTe₂ monolayer: Suppressed charge ordering and electric field tuned topological phase transition

Xiaoyin Li ^{1,2} Feng Liu ^{2,*} and Qian Wang^{1,†}

¹*Center for Applied Physics and Technology, Department of Materials Science and Engineering, HEDPS, and BKL-MEMD, College of Engineering, Peking University, Beijing 100871, China*

²*Department of Materials Science and Engineering, University of Utah, Salt Lake City, Utah 84112, USA*

 (Received 7 September 2020; revised 28 October 2020; accepted 2 November 2020; published 12 November 2020)

Two-dimensional materials with atomic thickness usually possess superior tunability by surface adsorption than their bulk counterparts, showing great promise for novel nanotechnologies. In layered transition-metal dichalcogenide IrTe₂ there exhibits complex structural distortions induced by charge ordering, resulting in difficulties for the applications of its corresponding monolayer material. Here, using first-principles calculations, we demonstrate that depositing Na on the surface of the IrTe₂ monolayer can suppress the structural distortion to form a stable NaIrTe₂ sheet. It naturally breaks the inversion symmetry to enable a Rashba-type spin splitting for potential spintronic applications. In addition, the introduced empty Na *s* band and the valence band of the IrTe₂ monolayer can be inverted by the application of a perpendicular electric field, achieving a quantum phase transition from normal to topological insulator. Such an electric field-controlled topological phase transition is promising for the realization of topological field-effect transistors. These findings not only provide a feasible approach to stabilizing the IrTe₂ monolayer, but also broaden its applications in spintronics and low-dissipation topoelectronics.

DOI: [10.1103/PhysRevB.102.195420](https://doi.org/10.1103/PhysRevB.102.195420)

I. INTRODUCTION

Since the successful exfoliation of graphene in 2004 [1], a vast number of layered materials have been thinned down to monolayers [2]. These two-dimensional (2D) materials possess compelling physical, chemical, electronic, and optical properties that are not found in their bulk counterparts, showing great promise for wide applications [3]. Furthermore, one distinct advantage of 2D materials over their bulk counterparts is their superior tunability, in particular due to their “ultrathin-ness” and large surface area. The ultrathin-ness, down to one single atomic layer, makes 2D materials more amenable to strain engineering [4] because they can sustain much larger tensile strain than bulk [5]. The large surface area, up to an infinite surface to volume ratio, equips 2D materials with ease of doping with surface adsorption [6–8] as well as modifying their properties, such as inducing structural and electronic phase transitions [9,10]. Also, the 2D materials’ properties have been shown to be strongly dependent on external electrical and magnetic fields [11–13]. Here, we demonstrate a unique and interesting example of “one stone killing two birds” manifested by the high tunability of 2D materials, where surface adsorption, on the one hand, stabilizes an otherwise unstable 2D material, and on the other hand, creates new properties to broaden its applications.

Transition-metal dichalcogenide (TMD) IrTe₂ is a typical layered material adopting the high-symmetric 1T structure at the room temperature, which has received much attention, especially on its bulk [14–22], cleaved surfaces [23–26], and

thin flakes [27–29] because of the intriguing properties including large spin-orbit coupling (SOC), charge-ordering phase transitions, as well as the emergence of superconductivity. Based on these features of IrTe₂, we envision that the corresponding monolayer would present unprecedented properties. However, the investigation and the subsequent application of the IrTe₂ monolayer are challenging, primarily due to the poor stability and the intricate charge-ordering behaviors of this material. To our knowledge, only the substrate-supported IrTe₂ monolayer has been reported so far, where the monolayer is strongly hybridized with the underneath Ir(111) substrate, which severely mitigates its 2D character [30]. Therefore, it is highly desirable and of importance to stabilize the IrTe₂ monolayer and explore its potential applications.

It is noteworthy that carrier doping has been verified as an effective approach to stabilizing the charge-ordering systems and suppressing the associated structural phase transition [31–35]. Indeed, previous studies have demonstrated that *n*-type Pt, Pd, or Cu doping can significantly suppress the charge ordering-induced monoclinic phase transition in bulk IrTe₂ [36–39]. However, these dopants will introduce a large number of valence electrons overwhelming the electronic property of the host monolayer, hindering the exploration of intrinsic properties of the IrTe₂ monolayer. Besides the *n*-type doping, another promising strategy is alkali metal deposition or intercalation [9,40,41]. Electrons transfer from the alkali metal atoms to the host system, thus altering the electronic band filling and phase stability of the system. Especially, it was found that Na atom intercalation can remove the soft phonon modes and suppress the structural instability of a typical charge-ordering system, like the bilayer NbSe₂ [42]. These findings are inspiring and have motivated us to explore the

*fliu@eng.utah.edu

†qianwang2@pku.edu.cn

possibility of stabilizing the IrTe_2 monolayer using the same strategy.

In this work, using first-principles calculations, we demonstrate that surface adsorption of Na atoms indeed stabilizes the IrTe_2 monolayer by suppressing its structural distortion. Also, the addition of Na atoms naturally breaks the inversion symmetry of the IrTe_2 monolayer, giving rise to a large spin splitting originated from Rashba SOC. Moreover, a perpendicular electric field can efficiently tune the electronic properties of the newly formed NaIrTe_2 sheet, inducing a topological phase transition from a normal insulator to a topological insulator. The underlying mechanism of the topological phase transition is uncovered by using a tight-binding model analysis.

II. COMPUTATIONAL METHODS

All first-principles calculations are performed in the framework of density-functional theory (DFT) as implemented in the Vienna *Ab initio* Simulation Package (VASP) [43]. The electron-ion interactions are described using the projector augmented-wave method [44]. The exchange-correlation interactions are treated by adopting the Perdew-Burke-Ernzerhof functional within the generalized gradient approximation [45]. The plane-wave energy cutoff is set to 500 eV, and a Γ -centered k -point mesh with a grid density of $2\pi \times 0.02 \text{ \AA}^{-1}$ is used for the Brillouin-zone integrations [46]. Lattice parameters and atomic positions are fully relaxed, and the convergence criteria for energy and force are set to 10^{-5} eV and 10^{-3} eV/ \AA , respectively. A vacuum space of 20 \AA in the direction perpendicular to the sheet is placed to avoid interactions between the periodic images. The convergence thresholds are raised to 10^{-8} eV and 10^{-6} eV/ \AA for phonon calculations, which are performed using the finite displacement method implemented in the PHONOPY package [47]. SOC is taken into account, and the topological edge states are calculated using the iterative Green function method [48–50].

III. RESULTS AND DISCUSSION

The optimized structure of the Na-adsorbed IrTe_2 monolayer is shown in Fig. 1(a), where each unit cell of the IrTe_2 monolayer accommodates one Na atom forming a stoichiometric NaIrTe_2 sheet. The resulting NaIrTe_2 monolayer has a 2D hexagonal lattice, with the lattice parameter of 4.11 \AA . It consists of four triangular atomic layers stacked along the z direction in the sequence of Te-Ir-Te-Na. The Te-Ir-Te layers maintain the original *ABC* stacking order, i.e., the 1*T* structure of IrTe_2 [15], while the Na atoms are located on top of Ir atoms. Apparently, the presence of the topmost Na layer breaks the structural inversion symmetry possessed by 1*T*- IrTe_2 , and the space-group symmetry of NaIrTe_2 reduces to $P3m1$ (No. 156) from $P-3m1$ (No. 164) of 1*T*- IrTe_2 . More structural details are given in Table S1 in the Supplemental Material (SM) [51].

To assess the effect of Na adsorption on the structural stability of the IrTe_2 monolayer, we calculate the phonon spectra of NaIrTe_2 , as shown in Fig. 1(b). There is no imaginary mode in the entire Brillouin zone, indicating that NaIrTe_2 is dynamically stable. In contrast, the calculated phonon spectra

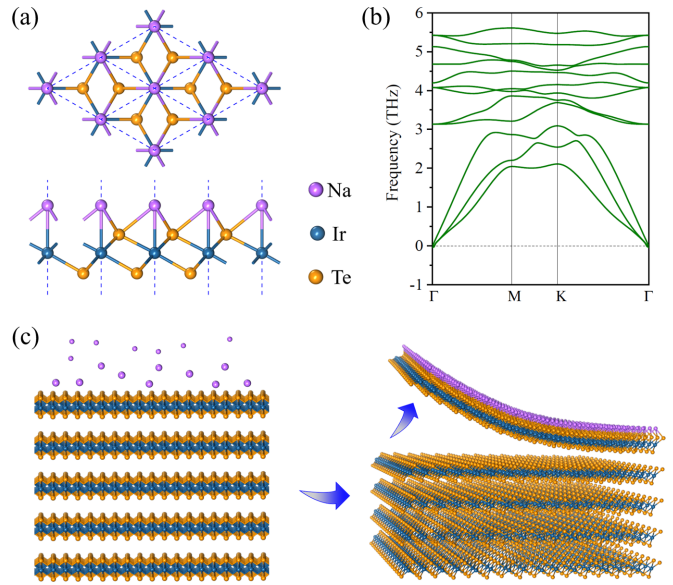


FIG. 1. (a) Top and side views of the optimized structure of NaIrTe_2 . The blue dashed lines outline the unit cell. (b) The phonon spectra of NaIrTe_2 . (c) Schematic of possible synthesis process of NaIrTe_2 .

of the pristine IrTe_2 monolayer exhibit three imaginary modes (see Fig. S1 [51]), suggesting that the IrTe_2 monolayer is dynamically unstable and lattice distortions are expected at low temperature. This comparison indicates that the Na adsorption can mitigate the structural instability of the IrTe_2 monolayer. Recently, Pb deposition has been successfully demonstrated on the cleaved IrTe_2 surfaces by epitaxial growth process, where the growth mode depends on the deposition temperature [52]. In particular, when deposited at room temperature, a uniform Pb film forms on the IrTe_2 substrate which adopts the high-symmetric 1*T* structure. Similarly, we suggest that it is possible to synthesize NaIrTe_2 by using the same method, as depicted in Fig. 1(c). After the Na atoms are deposited on the surface of IrTe_2 to form a uniform film, the topmost monolayer might be exfoliated [27], to obtain the NaIrTe_2 sheet.

The mechanism for stabilizing the IrTe_2 monolayer by Na adsorption can be understood by analyzing the Na-induced change of electronic properties. Figures 2(a) and 2(b) show the band structures of the pristine IrTe_2 monolayer and NaIrTe_2 without the consideration of SOC. One can see that after depositing Na atoms, the system transforms from a metal to a semiconductor with a band gap of 0.41 eV, thus eliminating the charge density at the Fermi level along with the associated charge-ordering properties. The main factor driving this transition is the doping effect of Na atoms which donate electrons to the IrTe_2 monolayer to shift its Fermi level into the band gap. Bader charge analysis [53] shows that each Na atom denotes ~ 0.7 electrons to the monolayer, suggesting that Na atoms are nearly fully ionized, which is consistent with the band-structure result. Along with this metal to semiconductor transition, the introduced Na s band, positioned at the original band-gap region, forms the conduction band (see Fig. S2 for detail [51]), resulting in a smaller band gap.

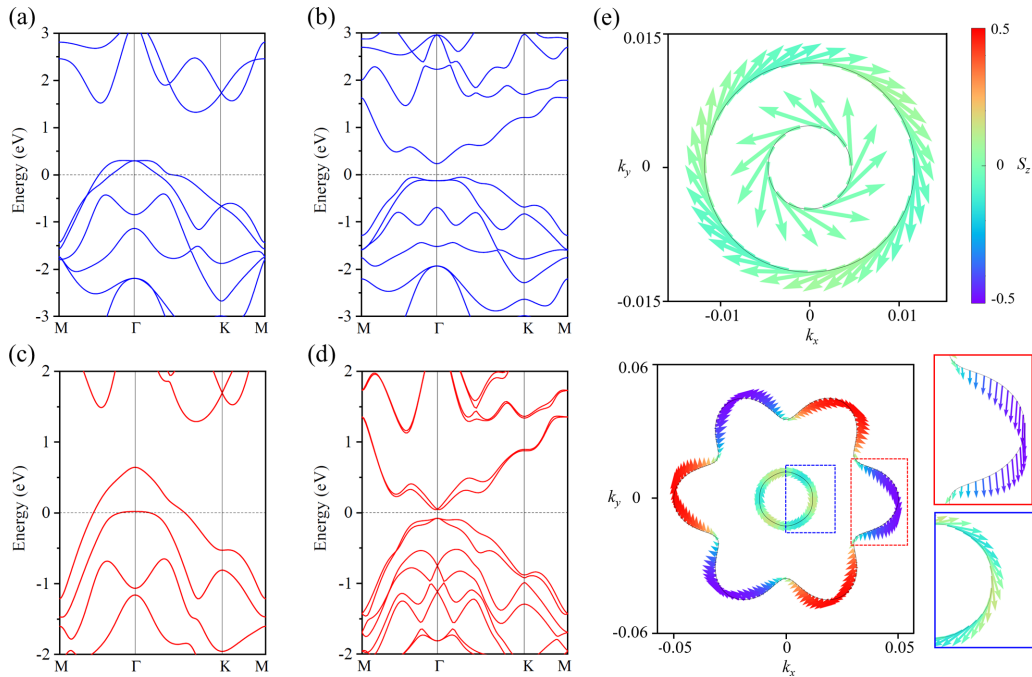


FIG. 2. Band structure of (a) the IrTe₂ monolayer and (b) NaIrTe₂ excluding SOC. Band structure of (c) the IrTe₂ monolayer and (d) NaIrTe₂ including SOC. (e) Spin textures of NaIrTe₂ bands at the constant energy surfaces $E = 0.1$ eV (top panel) and $E = -0.1$ eV (bottom panel); the arrows represent $[S_x(\mathbf{k}), S_y(\mathbf{k})]$ and the color map reflects the value of $S_z(\mathbf{k})$. The Fermi energy is set to zero.

Since large SOC is one of the predominant properties of IrTe₂, we next investigate the electronic structures with consideration of SOC. As shown in Fig. 2(c), for the pristine IrTe₂ monolayer some originally degenerate points are opened, but all bands still hold spin degeneracy due to the coexistence of time reversal and inversion symmetries. However, for NaIrTe₂ the inversion symmetry is broken, leading to the lifted spin degeneracy and large band splitting, as shown in Fig. 2(d). Accordingly, the band gap is reduced to 0.12 eV. More importantly, Na adsorption results in a potential asymmetry perpendicular to the 2D plane, which is expected to originate Rashba SOC effect [54]. To confirm this, we calculate the spin textures of bands near the Fermi level [55], since these bands are more accessible by experiments. For an eigenstate $\psi(\mathbf{k})$, its spin polarization at the \mathbf{k} point is defined as $S(\mathbf{k}) = [S_x(\mathbf{k}), S_y(\mathbf{k}), S_z(\mathbf{k})]$, where $S_i(\mathbf{k}) = \langle \psi(\mathbf{k}) | \sigma_i | \psi(\mathbf{k}) \rangle$ is the i -direction component and σ_i is the Pauli matrix ($i = x, y, z$). Figure 2(e) presents the calculated results at the constant energy surfaces $E = 0.1$ and -0.1 eV, respectively. One can see that for the conduction bands, the S_z component of the spin polarization is negligible and the xy -plane spin polarization is nearly perpendicular to its momentum, which is exactly the characteristic spin texture of Rashba SOC, whereas for the valence bands, all three spin components S_x , S_y , and S_z have sizable values at the constant energy surface. This difference is attributed to the different orbital compositions of the conduction and valence bands of NaIrTe₂. From the aforementioned results, the conduction bands mainly come from Na s orbital, where the out of plane asymmetric potential plays a dominant role in driving the spin splitting and gives rise to the Rashba-type spin texture. However, the valence bands are from the IrTe₂ monolayer, composed of multiorbitals including Ir d and Te p orbitals [28] that experience not only

the out-of-plane potential asymmetry but also the in-plane potential-energy gradient, resulting in spin polarizations with nonzero S_z components. Rashba SOC is central to various spintronic applications, and its performance is determined to a large extent by the strength of SOC and the purity of the states [56]. Here in NaIrTe₂, the Na adsorption-induced Rashba states are calculated to have the Rashba coefficient of $\lambda = 0.67$ eV Å (0.64 eV Å) along the Γ - M (Γ - K) direction (see Fig. S3 in the SM for details [51]), which is comparable to those of heavy-metal surface systems [57]. Moreover, the induced Rashba states are completely separated from other states, providing an ideal platform for exploring and realizing the high-performance spintronic devices.

Considering the fact that 2D materials with large SOC are good candidates for realizing the quantum spin Hall (QSH) effect, we calculate the Z_2 invariant of NaIrTe₂ to explore its topological nature. However, the calculated result of $Z_2 = 0$ suggests that NaIrTe₂ is a topological trivial normal insulator [see Fig. 3(a)]. On the other hand, it is known that perturbations such as strain and electric field can effectively tune the electronic properties of 2D materials. Especially, it was reported that a perpendicular electric field can convert the few-layer phosphorene from a normal insulator to a topological insulator [58]. Is it possible to achieve a similar topological phase transition in NaIrTe₂ with the assistance of an electric field? To answer this question, we investigate the electronic properties of NaIrTe₂ under a perpendicular electric field. Figure 4(a) shows the band gap of NaIrTe₂ as a function of the electric field E_z . Clearly, there is a band-gap closure and reopen process where the topological phase transition is supposed to happen. As the applied electric field increases, the band gap of NaIrTe₂ decreases almost linearly until it vanishes at a critical electric field $E_z = 0.34$ V/Å, where the

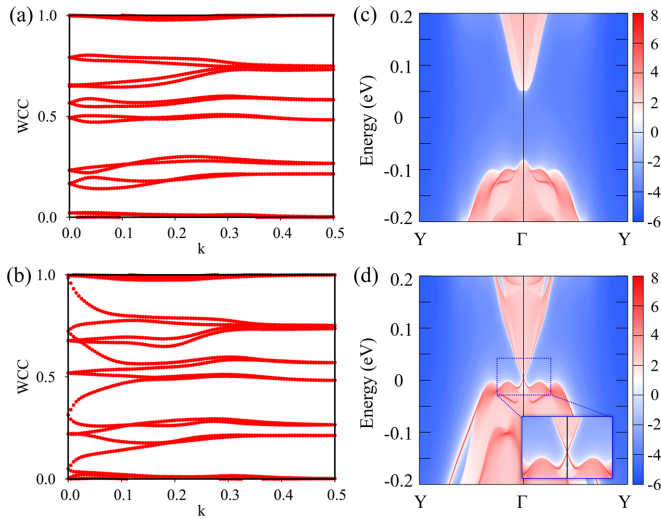


FIG. 3. Wannier Charge Center (WCC) evolutions for NaIrTe₂ with the perpendicular electric field of (a) $E_z = 0$ and (b) $E_z = 0.45 \text{ V/\AA}$. For an arbitrary reference line parallel to the k axis, the WCC evolutions will cross it even/odd number of times for $Z_2 = 0/1$. Consequently, one obtains $Z_2 = 0$ for (a) $E_z = 0$, and $Z_2 = 1$ for (b) $E_z = 0.45 \text{ V/\AA}$. (c), (d) Semi-infinite edge states of NaIrTe₂ under the electric field of $E_z = 0$ and 0.45 V/\AA , respectively. The color bar represents the magnitude of the projected edge density of states, which is dimensionless and obtained from the imaginary part of the edge Green function: $A(k_{//}, \omega) = -\frac{1}{\pi} \lim_{\eta \rightarrow 0^+} \text{ImTr}G_s(k_{//}, \omega + i\eta)$, where $k_{//}$ is the momentum along the edge and ω is the energy [49]. Blue, white, and red colors are for low, medium, and high edge density of states, respectively.

conduction and valence bands touch each other at the Γ point, as shown in Fig. 4(b) and Fig. S4. When further increasing the electric field, the band gap reopens and increases to 18 meV at the electric field $E_z = 0.4 \text{ V/\AA}$. Note that for $E_z > 0.4 \text{ V/\AA}$, the band gap remains nearly constant (18 meV for $E_z = 0.45 \text{ V/\AA}$ and 14 meV for $E_z = 0.5 \text{ V/\AA}$) because the valence-band maximum of NaIrTe₂ shifts away from the Γ point in this range of field, which makes the global band gap nearly unchanged (see Fig. S4 for details [51]). The three-dimensional (3D) conduction and valence bands of NaIrTe₂ under the electric field of 0, 0.34, and 0.45 V/\AA are calculated and plotted in Fig. 4(b), further confirming the electric field-induced band-gap closure and reopen process. To verify the existence of a topological phase transition, we calculated the Z_2 invariant of NaIrTe₂ under $E_z = 0.45 \text{ V/\AA}$ and found $Z_2 = 1$ [see Fig. 3(b)] indicating a topological insulator. These results demonstrate that a perpendicular electric field can indeed tune NaIrTe₂ from a normal insulator into a 2D topological insulator, i.e., a QSH insulator, and the critical field for this topological phase transition is 0.34 V/\AA . Accordingly, a topological phase diagram of NaIrTe₂ can be constructed as shown in Fig. 4(a). We notice that the proposed magnitude of electric field is within the reach of current experimental techniques [59], implying the feasibility of using electric field to tune topological phase transition in NaIrTe₂.

It is well known that one of the remarkable properties of 2D topological insulators is the existence of the robust gapless edge states located inside the bulk gap. Therefore,

the edge-energy spectra of the semi-infinite NaIrTe₂ under different electric fields are calculated. Figure 3(c) displays the result without the electric field ($E_z = 0$), where the bulk conduction and valence bands are completely separated from each other by a charge gap. In contrast, at $E_z = 0.45 \text{ V/\AA}$, the Dirac-like edge states are clearly seen to connect the bulk conduction and valence bands, as shown in Fig. 3(d). These results again confirm the topological phase transition of NaIrTe₂ induced by the electric field, in agreement with the topological invariant results. Actually, such electric field-controlled topological phase transition is highly desirable for the realization of the topological field-effect transistors, where the on/off state corresponds to the appearance/disappearance of quantized edge conductance [60]. Therefore, we propose a topological field-effect transistor device made of dual-gated NaIrTe₂, as shown in Fig. 4(c). Using the two gates, one can tune the Fermi level of the device and the topological phase transition of NaIrTe₂ independently. When the Fermi level is tuned to reside in the bulk band gap, the on/off state of the device can be controlled by the perpendicular electric field solely. In the absence of the perpendicular electric field, NaIrTe₂ is a normal insulator without the conducting edge states, hence the device performs as off state. When applying a perpendicular electric field $E_z > 0.34 \text{ V/\AA}$, NaIrTe₂ becomes a topological insulator robustly conducting along the edges, and the device is switched to on state. It is worth noting that the topological edge states can be gapped by finite-size effect in QSH insulator nanoribbons due to the interactions between left and right edge states [61]. Therefore, a sufficiently large width of the NaIrTe₂ nanoribbon is required to measure the conducting edge states. Based on the previous study of 1T'-TMD monolayers, where the edge states have a decay length of $\sim 5 \text{ nm}$ and the minimum width of the device is about 20 nm [62], we expect that the proposed device in this study should have a similar width to guarantee its performance.

The underlying mechanism for the topological phase transition of NaIrTe₂ can be further clarified with an effective model Hamiltonian. It is noteworthy to point out that it is the band evolution at the Γ point that determines the topological phase transition of NaIrTe₂, as shown in Fig. 4(b). Therefore, one can focus on the bands near the Γ point. For simplicity, we first construct the model without consideration of SOC. In this situation, only two occupied and one unoccupied states are involved in the band inversion; therefore, a minimal three-band model is sufficient to capture the essential physics. From the band decomposed charge density of NaIrTe₂ as shown in Fig. S5 of the SM [51], at the Γ point, the conduction state mostly consists of Na s orbital while the degenerate valence states are mainly contributed by the Te p_x and p_y orbitals. Considering that the charge density of the valence bands has the shape of p_x/p_y orbitals but is branched over both the top and bottom Te atoms [51], to mimic their parity character, one may use a single set of (p_x, p_y) orbitals centered on the Ir site as a replicating basis to construct the minimal model. Consequently, the two pseudo- p_x and p_y orbitals along with the Na s orbital constitute a trigonal lattice as shown in Fig. 5(a), which was shown to be the minimum-basis model required for topological state in a trigonal lattice [63]. Accordingly, the spinless tight-binding (TB) Hamiltonian can be

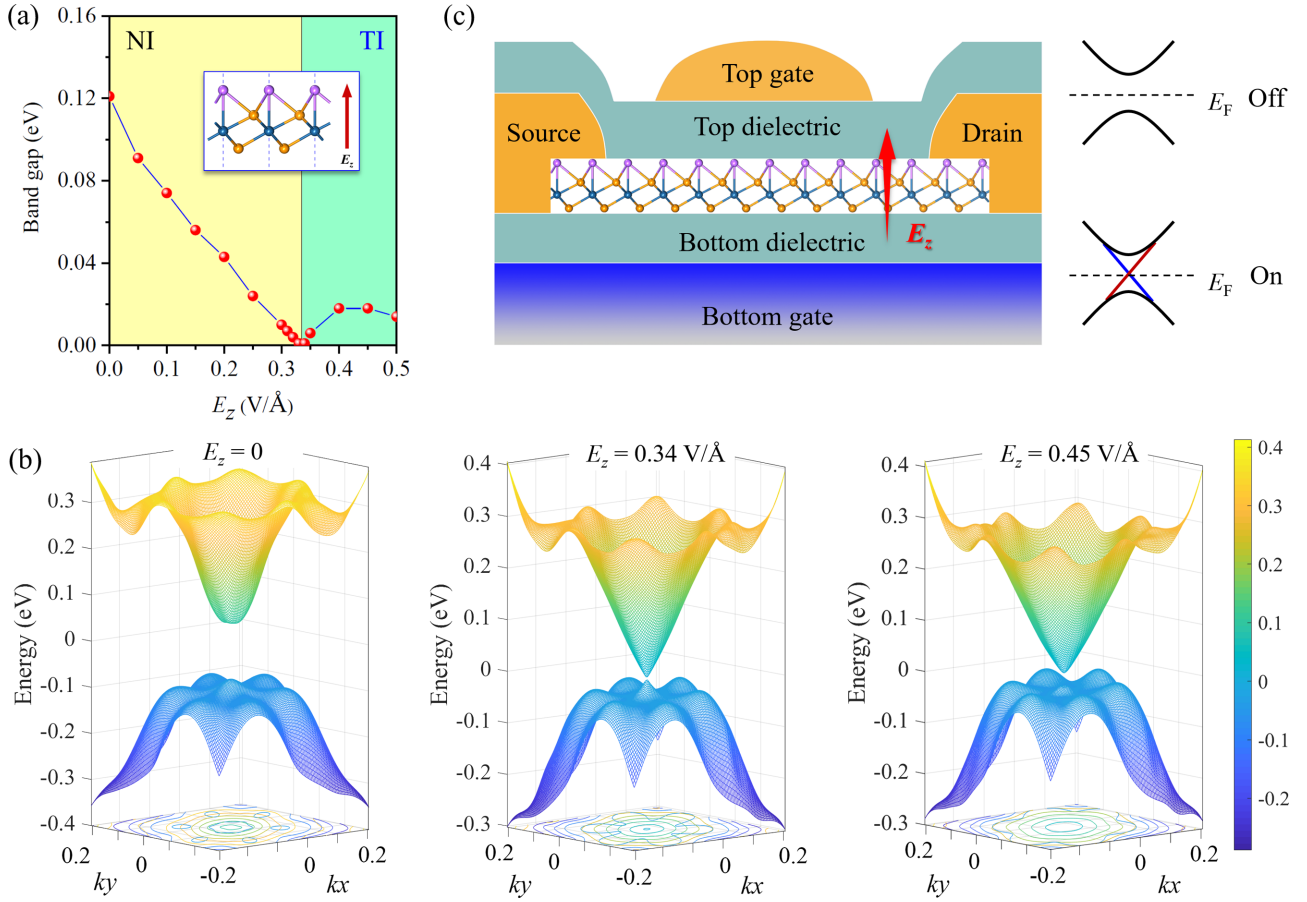


FIG. 4. (a) Band gap of NaIrTe₂ as a function of the electric field. (b) 3D conduction and valence bands of NaIrTe₂ with an electric field of 0, 0.34, and 0.45 V/Å, respectively. The color bar indicates the energy of bands in unit of eV. (c) Schematic of the topological field-effect transistor device based on NaIrTe₂. E_F represents the Fermi level.

written as

$$H_0 = \sum_{\alpha} \varepsilon_{\alpha} c_{0\alpha}^{\dagger} c_{0\alpha} + \sum_i \sum_{\alpha, \beta} (t_{0\alpha, i\beta} c_{0\alpha}^{\dagger} c_{i\beta} + t_{i\beta, 0\alpha} c_{i\beta}^{\dagger} c_{0\alpha}), \quad (1)$$

where $\alpha, \beta = s, p_x, p_y$ are the orbital indices, ε_{α} is the on-site energy, c^{\dagger} and c are the creation and annihilation operators, and $t_{0\alpha, i\beta}$ is the hopping parameter. By including the nearest-neighbor (NN) and the next-NN (NNN) hoppings, the TB

model reproduces well the essential features of the conduction and valence bands of NaIrTe₂, as shown in Fig. 5(b), and the Hamiltonian reads as

$$H_0 = \begin{pmatrix} h_{11} & h_{12} & h_{13} \\ h_{12}^* & h_{22} & h_{23} \\ h_{13}^* & h_{23}^* & h_{33} \end{pmatrix}, \quad (2)$$

with matrix elements of

$$h_{11} = \varepsilon_s + t_{ss\sigma 1} \left(4 \cos \frac{\sqrt{3}}{2} k_x \cos \frac{1}{2} k_y + 2 \cos k_y \right) + t_{ss\sigma 2} \left(4 \cos \frac{\sqrt{3}}{2} k_x \cos \frac{3}{2} k_y + 2 \cos \sqrt{3} k_x \right)$$

$$h_{12} = 2\sqrt{3} i t_{sp\sigma 1} \sin \frac{\sqrt{3}}{2} k_x \cos \frac{1}{2} k_y + 2 i t_{sp\sigma 2} \sin \sqrt{3} k_x + 2 i t_{sp\sigma 2} \sin \frac{\sqrt{3}}{2} k_x \cos \frac{3}{2} k_y$$

$$h_{13} = 2 i t_{sp\sigma 1} \left(\cos \frac{\sqrt{3}}{2} k_x \sin \frac{1}{2} k_y + \sin k_y \right) + 2\sqrt{3} i t_{sp\sigma 2} \sin \frac{3}{2} k_y \cos \frac{\sqrt{3}}{2} k_x$$

$$h_{22} = \varepsilon_p + (3t_{pp\sigma 1} + t_{pp\pi 1}) \cos \frac{\sqrt{3}}{2} k_x \cos \frac{1}{2} k_y + 2t_{pp\pi 1} \cos k_y + 2t_{pp\sigma 2} \cos \sqrt{3} k_x + (t_{pp\sigma 2} + 3t_{pp\pi 2}) \cos \frac{\sqrt{3}}{2} k_x \cos \frac{3}{2} k_y$$

$$h_{23} = (t_{pp\pi 1} - t_{pp\sigma 1}) \sqrt{3} \sin \frac{\sqrt{3}}{2} k_x \sin \frac{1}{2} k_y + \sqrt{3} (t_{pp\pi 2} - t_{pp\sigma 2}) \sin \frac{\sqrt{3}}{2} k_x \sin \frac{3}{2} k_y$$

$$h_{33} = \varepsilon_p + (t_{pp\sigma 1} + 3t_{pp\pi 1}) \cos \frac{\sqrt{3}}{2} k_x \cos \frac{1}{2} k_y + 2t_{pp\sigma 1} \cos k_y + (3t_{pp\sigma 2} + t_{pp\pi 2}) \cos \frac{\sqrt{3}}{2} k_x \cos \frac{3}{2} k_y + 2t_{pp\pi 2} \cos \sqrt{3} k_x.$$

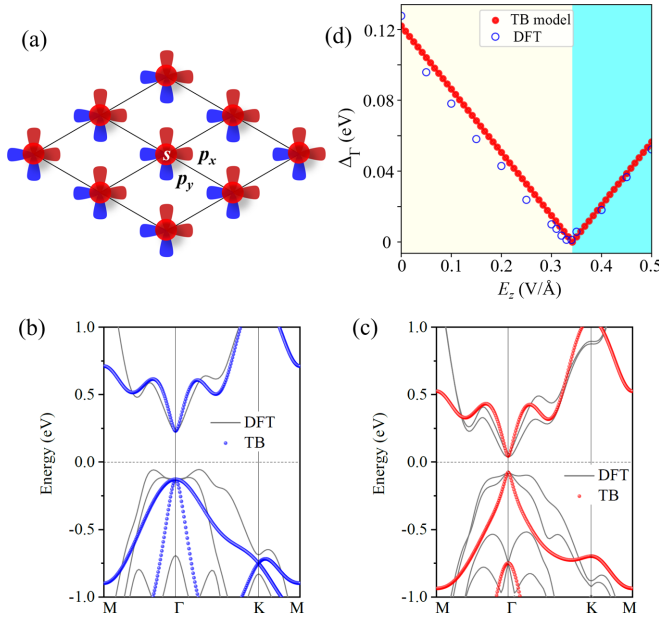


FIG. 5. (a) Trigonal lattice with three orbitals per lattice site, namely s , p_x , and p_y orbitals. The blue and red colors indicate the different lobes of p orbitals with distinct phases. TB band structures of NaIrTe₂ without (b) and with (c) SOC. (d) The Γ -point band gap Δ_Γ of NaIrTe₂ as a function of the electric field. The blue hollow circles are the first-principles calculation results; the red solid circles are the TB results.

Here, ε_s and ε_p are on-site energies for s - and p -orbitals, $t_{ss\sigma}$, $t_{sp\sigma}$, $t_{pp\sigma}$, and $t_{pp\pi}$ are hopping parameters, and the subscript 1/2 indicates the NN/NNN hopping. The model parameters are derived by fitting the TB bands to the DFT results, which are listed in Table I.

When SOC is taken into account, a two-step simplification is required to make this problem easier. First, as noted above, the topological phase transition of NaIrTe₂ is determined by the band evolution at the Γ point, where Rashba SOC vanishes and the spin degeneracy is conserved (Kramers' degeneracy). Thus, one can reasonably neglect the Rashba SOC term and only include the on-site SOC term to the Hamiltonian, written as

$$H_{\text{SOC}} = -i\lambda(c_{0p_x}^\dagger c_{0p_y} - c_{0p_y}^\dagger c_{0p_x})s_z. \quad (3)$$

Here λ is the SOC strength, s_z is the Pauli matrix, and i is the imaginary unit. Herein, the spin-up and spin-down bands are degenerate everywhere and the spin-up and spin-down Hamiltonians can be decoupled. Therefore, we focus on the spin-up part for further analysis while the spin-down part just leads to the same result. Consequently, the spin-up

TABLE I. The model parameters of NaIrTe₂, including the on-site energy ε (eV), the hopping parameter t (eV), and the SOC strength λ (eV).

ε_s	ε_p	$t_{ss\sigma 1}$	$t_{ss\sigma 2}$	$t_{sp\sigma 1}$	$t_{sp\sigma 2}$	$t_{pp\sigma 1}$	$t_{pp\sigma 2}$	$t_{pp\pi 1}$	$t_{pp\pi 2}$	λ
0.405	-1.070	-0.113	0.053	0.133	0.093	0.137	0.082	0.001	-0.001	0.336

Hamiltonian is written as

$$H = H_0 + H_{\text{SOC}} = \begin{pmatrix} h_{11} & h_{12} & h_{13} \\ h_{12}^* & h_{22} & h_{23} \\ h_{13}^* & h_{23}^* & h_{33} \end{pmatrix} + \begin{pmatrix} 0 & 0 & 0 \\ 0 & 0 & -i\lambda \\ 0 & i\lambda & 0 \end{pmatrix}. \quad (4)$$

By fitting the DFT bands, the value of λ is derived as listed in Table I. The resulting TB bands are plotted in Fig. 5(c), showing good agreement with the DFT results.

At the Γ point, by diagonalizing the above Hamiltonian one obtains three eigenvalues of $E_s = \varepsilon_s + 6(t_{ss\sigma 1} + t_{ss\sigma 2})$ and $E_p^{\pm\lambda} = \varepsilon_p + 3(t_{pp\sigma 1} + t_{pp\sigma 2} + t_{pp\pi 1} + t_{pp\pi 2}) \pm \lambda$, respectively. Hence, the band gap at the Γ point is

$$\Delta_\Gamma = E_s - E_p^{+\lambda} = (\varepsilon_s - \varepsilon_p) - \lambda + [6(t_{ss\sigma 1} + t_{ss\sigma 2}) - 3(t_{pp\sigma 1} + t_{pp\sigma 2} + t_{pp\pi 1} + t_{pp\pi 2})]. \quad (5)$$

The application of a perpendicular electric field will add a z -dependent potential energy to the system, which can be incorporated in the model Hamiltonian through the on-site energy terms. Orbitals in different layers experience different potential energy, resulting in the relative energy shift approximately expressed as $\delta = -\gamma E_z$, where E_z is the electric field and γ is proportional to the interlayer distance d as $\gamma = ed$ [58]. Adding this term to the model Hamiltonian, one can obtain Δ_Γ as a function of the electric field E_z as

$$\Delta_\Gamma = E_s - E_p^{+\lambda} = (\varepsilon_s - \varepsilon_p - \gamma E_z) - \lambda + [6(t_{ss\sigma 1} + t_{ss\sigma 2}) - 3(t_{pp\sigma 1} + t_{pp\sigma 2} + t_{pp\pi 1} + t_{pp\pi 2})]. \quad (6)$$

The value of γ can be derived by substituting $E_z = 0.34 \text{ V/\AA}$, $\Delta_\Gamma = 0$ into Eq. (6), yielding a result of 0.357 e\AA . So far, all parameters have been given, based on which we plot the Γ -point band gap Δ_Γ versus the electric field E_z in Fig. 5(d). It shows that as the electric field increases, the band gap firstly decreases until $\Delta_\Gamma = 0$. After that, the energy order of E_s and $E_p^{+\lambda}$ reverses and the band gap begins to increase with the increasing electric field. Clearly, it is the inversion of E_s and $E_p^{+\lambda}$ bands of opposite parity that induces the topological phase transition of NaIrTe₂, in agreement with previous model analysis [63]. In this sense, NaIrTe₂ offers a realistic material system to realize the QSH effect in a trigonal lattice, shedding insights on the search and design of QSH insulators. We also plot the DFT results of Δ_Γ versus E_z , as shown in Fig. 5(d), which are in good agreement with those obtained from the TB model, validating the accuracy of this model.

IV. CONCLUSIONS

In summary, by using first-principles calculations, we demonstrate that surface adsorption of Na atoms on the IrTe₂ monolayer can suppress the charge ordering-induced structural distortion, forming a stable NaIrTe₂ monolayer with

the threefold rotational symmetry preserved. Furthermore, the Na overlayer breaks inversion symmetry and introduces ideal Rashba states that locate inside the band-gap region of the pristine IrTe₂ monolayer, while the energy order of the Na *s* band and the Te *p* band can be parity inverted by a perpendicular electric field to realize a topological phase transition from a normal insulator to a QSH insulator. These properties significantly broaden the application of the IrTe₂ monolayer for spintronics and low-dissipation devices. We hope that our findings will motivate further experimental explorations.

ACKNOWLEDGMENTS

This work is partially supported by grants from the National Key Research and Development Program of China (Grant No. 2017YFA0205003), and the National Natural Science Foundation of China (Grants No. 21773004 and No. 11974028). F.L. acknowledges support from US DOE-BES (Grant No. DE-FG02-04ER46148). Computations of this work were supported by the High Performance Computing Platform of Peking University.

-
- [1] K. S. Novoselov, A. K. Geim, S. V. Morozov, D. Jiang, Y. Zhang, S. V. Dubonos, I. V. Grigorieva, and A. A. Firsov, *Science* **306**, 666 (2004).
- [2] M. Chhowalla, H. S. Shin, G. Eda, L.-J. Li, K. P. Loh, and H. Zhang, *Nat. Chem.* **5**, 263 (2013).
- [3] C. Tan, X. Cao, X.-J. Wu, Q. He, J. Yang, X. Zhang, J. Chen, W. Zhao, S. Han, G.-H. Nam, M. Sindoro, and H. Zhang, *Chem. Rev.* **117**, 6225 (2017).
- [4] C. Si, Z. Sun, and F. Liu, *Nanoscale* **8**, 3207 (2016).
- [5] Y. Zhang and F. Liu, *Appl. Phys. Lett.* **99**, 241908 (2011).
- [6] Q. Fu and X. Bao, *Chem. Soc. Rev.* **46**, 1842 (2017).
- [7] T. Niu, J. Zhang, and W. Chen, *ChemNanoMat* **5**, 6 (2019).
- [8] P. Luo, F. Zhuge, Q. Zhang, Y. Chen, L. Lv, Y. Huang, H. Li, and T. Zhai, *Nanoscale Horiz.* **4**, 26 (2019).
- [9] M. Kan, J. Y. Wang, X. W. Li, S. H. Zhang, Y. W. Li, Y. Kawazoe, Q. Sun, and P. Jena, *J. Phys. Chem. C* **118**, 1515 (2014).
- [10] L. Gao, J.-T. Sun, G. Sethi, Y.-Y. Zhang, S. Du, and F. Liu, *Nanoscale* **11**, 22743 (2019).
- [11] A. F. Hebard and M. A. Paalanen, *Phys. Rev. Lett.* **65**, 927 (1990).
- [12] S. Misra, L. Urban, M. Kim, G. Sambandamurthy, and A. Yazdani, *Phys. Rev. Lett.* **110**, 037002 (2013).
- [13] F. Liu, J. Zhou, C. Zhu, and Z. Liu, *Adv. Funct. Mater.* **27**, 1602404 (2017).
- [14] H. Cao, B. C. Chakoumakos, X. Chen, J. Yan, M. A. McGuire, H. Yang, R. Custelcean, H. Zhou, D. J. Singh, and D. Mandrus, *Phys. Rev. B* **88**, 115122 (2013).
- [15] Y. S. Oh, J. J. Yang, Y. Horibe, and S. W. Cheong, *Phys. Rev. Lett.* **110**, 127209 (2013).
- [16] G. L. Pascut, T. Birol, M. J. Gutmann, J. J. Yang, S. W. Cheong, K. Haule, and V. Kiryukhin, *Phys. Rev. B* **90**, 195122 (2014).
- [17] G. L. Pascut, K. Haule, M. J. Gutmann, S. A. Barnett, A. Bombardi, S. Artyukhin, T. Birol, D. Vanderbilt, J. J. Yang, S. W. Cheong, and V. Kiryukhin, *Phys. Rev. Lett.* **112**, 086402 (2014).
- [18] M. J. Eom, K. Kim, Y. J. Jo, J. J. Yang, E. S. Choi, B. I. Min, J. H. Park, S. W. Cheong, and J. S. Kim, *Phys. Rev. Lett.* **113**, 266406 (2014).
- [19] D. Mazumdar, K. Haule, J. J. Yang, G. L. Pascut, B. S. Holinsworth, K. R. O'Neal, V. Kiryukhin, S.-W. Cheong, and J. L. Musfeldt, *Phys. Rev. B* **91**, 041105(R) (2015).
- [20] K. Kim, S. Kim, K. T. Ko, H. Lee, J. H. Park, J. J. Yang, S. W. Cheong, and B. I. Min, *Phys. Rev. Lett.* **114**, 136401 (2015).
- [21] G. Cao, W. Xie, W. A. Phelan, J. F. DiTusa, and R. Jin, *Phys. Rev. B* **95**, 035148 (2017).
- [22] G. Saleh and S. Artyukhin, *J. Phys. Chem. Lett.* **11**, 2127 (2020).
- [23] Q. Li, W. Lin, J. Yan, X. Chen, A. G. Gianfrancesco, D. J. Singh, D. Mandrus, S. V. Kalinin, and M. Pan, *Nat. Commun.* **5**, 5358 (2014).
- [24] H. S. Kim, S. Kim, K. Kim, B. I. Min, Y.-H. Cho, L. Wang, S.-W. Cheong, and H. W. Yeom, *Nano Lett.* **16**, 4260 (2016).
- [25] D. Ootsuki, H. Ishii, K. Kudo, M. Nohara, M. Takahashi, M. Horio, A. Fujimori, T. Yoshida, M. Arita, H. Anzai, H. Namatame, M. Taniguchi, N. L. Saini, and T. Mizokawa, *J. Phys. Soc. Jpn.* **86**, 123704 (2017).
- [26] C. Chen, J. Kim, Y. Yang, G. Cao, R. Jin, and E. W. Plummer, *Phys. Rev. B* **95**, 094118 (2017).
- [27] M. Yoshida, K. Kudo, M. Nohara, and Y. Iwasa, *Nano Lett.* **18**, 3113 (2018).
- [28] S.-i. Ideta, D. Zhang, A. G. Dijkstra, S. Artyukhin, S. Keskin, R. Cingolani, T. Shimojima, K. Ishizaka, H. Ishii, K. Kudo, M. Nohara, and R. J. D. Miller, *Sci. Adv.* **4**, eaar3867 (2018).
- [29] H. Oike, M. Kamitani, Y. Tokura, and F. Kagawa, *Sci. Adv.* **4**, eaau3489 (2018).
- [30] A. Wang, Z. Liu, J. Pan, Q. Li, G. Li, Q. Huan, S. Du, and H.-J. Gao, *Chin. Phys. B* **29**, 078102 (2020).
- [31] Y. Yu, F. Yang, X. F. Lu, Y. J. Yan, Y.-H. Cho, L. Ma, X. Niu, S. Kim, Y.-W. Son, D. Feng, S. Li, S.-W. Cheong, X. H. Chen, and Y. Zhang, *Nat. Nanotechnol.* **10**, 270 (2015).
- [32] L. J. Li, E. C. T. O'Farrell, K. P. Loh, G. Eda, B. Özyilmaz, and A. H. Castro Neto, *Nature (London)* **529**, 185 (2016).
- [33] X. Xi, H. Berger, L. Forró, J. Shan, and K. F. Mak, *Phys. Rev. Lett.* **117**, 106801 (2016).
- [34] B. Guster, E. Canadell, M. Pruneda, and P. Ordejón, *2D Mater.* **5**, 025024 (2018).
- [35] J. S. Zhou, L. Monacelli, R. Bianco, I. Errea, F. Mauri, and M. Calandra, *Nano Lett.* **20**, 4809 (2020).
- [36] S. Pyon, K. Kudo, and M. Nohara, *J. Phys. Soc. Jpn.* **81**, 053701 (2012).
- [37] D. Ootsuki, Y. Wakisaka, S. Pyon, K. Kudo, M. Nohara, M. Arita, H. Anzai, H. Namatame, M. Taniguchi, N. L. Saini, and T. Mizokawa, *Phys. Rev. B* **86**, 014519 (2012).
- [38] J. J. Yang, Y. J. Choi, Y. S. Oh, A. Hogan, Y. Horibe, K. Kim, B. I. Min, and S. W. Cheong, *Phys. Rev. Lett.* **108**, 116402 (2012).
- [39] M. Kamitani, M. S. Bahramy, R. Arita, S. Seki, T. Arima, Y. Tokura, and S. Ishiwata, *Phys. Rev. B* **87**, 180501(R) (2013).
- [40] A. König, K. Koepf, R. Schuster, R. Kraus, M. Knupfer, B. Büchner, and H. Berger, *Europhys. Lett.* **100**, 27002 (2012).
- [41] K. Rossnagel, *New J. Phys.* **12**, 125018 (2010).

- [42] C.-S. Lian, C. Si, J. Wu, and W. Duan, *Phys. Rev. B* **96**, 235426 (2017).
- [43] G. Kresse and J. Furthmüller, *Phys. Rev. B* **54**, 11169 (1996).
- [44] P. E. Blöchl, *Phys. Rev. B* **50**, 17953 (1994).
- [45] J. P. Perdew, K. Burke, and M. Ernzerhof, *Phys. Rev. Lett.* **77**, 3865 (1996).
- [46] H. J. Monkhorst and J. D. Pack, *Phys. Rev. B* **13**, 5188 (1976).
- [47] A. Togo, F. Oba, and I. Tanaka, *Phys. Rev. B* **78**, 134106 (2008).
- [48] A. A. Mostofi, J. R. Yates, Y.-S. Lee, I. Souza, D. Vanderbilt, and N. Marzari, *Comput. Phys. Commun.* **178**, 685 (2008).
- [49] Q. Wu, S. Zhang, H.-F. Song, M. Troyer, and A. A. Soluyanov, *Comput. Phys. Commun.* **224**, 405 (2018).
- [50] M. P. L. Sancho, J. M. L. Sancho, J. M. L. Sancho, and J. Rubio, *J. Phys. F: Met. Phys.* **15**, 851 (1985).
- [51] See Supplemental Material at <http://link.aps.org/supplemental/10.1103/PhysRevB.102.195420> for structural parameters of NaIrTe₂, optimized structure and phonon spectra of monolayer IrTe₂, Na-*s* orbital decomposed band structure of NaIrTe₂, calculations of Rashba coefficients of NaIrTe₂, band structures of NaIrTe₂ under different electric fields, and band-decomposed charge density of NaIrTe₂.
- [52] J. W. Park, H. S. Kim, T. Brumme, T. Heine, and H. W. Yeom, *Nat. Commun.* **11**, 815 (2020).
- [53] W. Tang, E. Sanville, and G. Henkelman, *J. Phys.: Condens. Matter* **21**, 084204 (2009).
- [54] E. I. Rashba, *Sov. Phys. Solid State* **2**, 1109 (1960).
- [55] U. Herath, P. Tavazde, X. He, E. Bousquet, S. Singh, F. Muñoz, and A. H. Romero, *Comput. Phys. Commun.* **251**, 107080 (2020).
- [56] W. Ming, Z. F. Wang, M. Zhou, M. Yoon, and F. Liu, *Nano Lett.* **16**, 404 (2016).
- [57] C. R. Ast, J. Henk, A. Ernst, L. Moreschini, M. C. Falub, D. Pacilé, P. Bruno, K. Kern, and M. Grioni, *Phys. Rev. Lett.* **98**, 186807 (2007).
- [58] Q. Liu, X. Zhang, L. B. Abdalla, A. Fazzio, and A. Zunger, *Nano Lett.* **15**, 1222 (2015).
- [59] T. Zhang, J. Ha, N. Levy, Y. Kuk, and J. Stroschio, *Phys. Rev. Lett.* **111**, 056803 (2013).
- [60] J. Liu, T. H. Hsieh, P. Wei, W. Duan, J. Moodera, and L. Fu, *Nat. Mater.* **13**, 178 (2014).
- [61] B. Zhou, H.-Z. Lu, R.-L. Chu, S.-Q. Shen, and Q. Niu, *Phys. Rev. Lett.* **101**, 246807 (2008).
- [62] X. Qian, J. Liu, L. Fu, and J. Li, *Science* **346**, 1344 (2014).
- [63] Z. F. Wang, K.-H. Jin, and F. Liu, *Nat. Commun.* **7**, 12746 (2016).